

Article

# Fine-Tuning the Optical Design of the Advanced Virgo+ Gravitational-Wave Detector Using Binary-Neutron Star Signals

Jonathon Baird \*  and Matteo Barsuglia

Astroparticule et Cosmologie, Université de Paris, CNRS, F-75013 Paris, France; barsu@apc.in2p3.fr

\* Correspondence: baird@apc.in2p3.fr

Received: 3 November 2020; Accepted: 3 December 2020; Published: 8 December 2020



**Abstract:** Advanced Virgo+ is a major upgrade of the Advanced Virgo gravitational-wave detector aiming to increase sensitivity in terms of binary neutron star (BNS) range by a factor 3–5 in the next few years. In this work, we present an optimization of the mirror transmittances for the second phase of the project (to be implemented for the O5 observation run) using a random walk algorithm implemented with the advGWINC software. In addition to BNS range, a post merger (PM) SNR is also used as a figure of merit to identify configurations that fine-tune the sensitivity curve, as a function of arm-cavity round trip losses.

**Keywords:** gravitational-waves; interferometric detectors; Virgo; binary neutron stars

## 1. Introduction

In the last five years since the first detection of a binary black hole merger [1], the Advanced Virgo (AdV) and Advanced LIGO detector network has expanded its contribution to gravitational-wave astronomy. After a series of detector upgrades, the network entered its third observation run (O3), beginning in April 2019 and ending in March 2020. A total of 39 new sources have been discovered in the first part of the run (from April 2019 to October 2019) and included in the second catalog of gravitational-wave transient sources (GWTC-2) [2], with exceptional events independently published [3–7]. The analysis is ongoing for the second part of the run.

The AdV gravitational wave detector [8], an upgraded version of the Virgo detector [9] situated in Cascina Italy, is a power-recycled, Michelson interferometer (ITF) with Fabry–Perot cavities in each 3 km arm. Following the end of O3, AdV will undergo another set of upgrades in two phases (phase I and phase II), before the fourth and fifth observation runs (O4 and O5). These enhancements will take the ITF from AdV to Advanced Virgo+ (AdV+). Each upgrade phase will produce a global reduction in the detector noise as shown in Figure 1 (taken from Figure 1 in [10]), where the O2 and current O3 measured sensitivity (blue and green) will be lowered into the two projected sensitivities (gray for O4 and purple for O5).

Phase I upgrades mainly aim to reduce quantum noise (QN) by implementing a signal recycling technique, frequency dependent squeezing, and a higher laser power. Phase II upgrades will see an additional reduction in QN by a further increase in input laser power, but will mainly focus on a reduction of coating Brownian thermal noise. This will be done by improving the mechanical properties of test mass coatings and increasing the laser beam spot size on cavity end mirrors, consequently requiring end mirrors to be replaced with mirrors of larger radius. In order to achieve a larger beam spot size on the end mirrors, all curved mirrors in the ITF will be replaced with mirrors polished to different radii of curvature (RoCs). The resulting optical layout for O5 is shown in Figure 2.

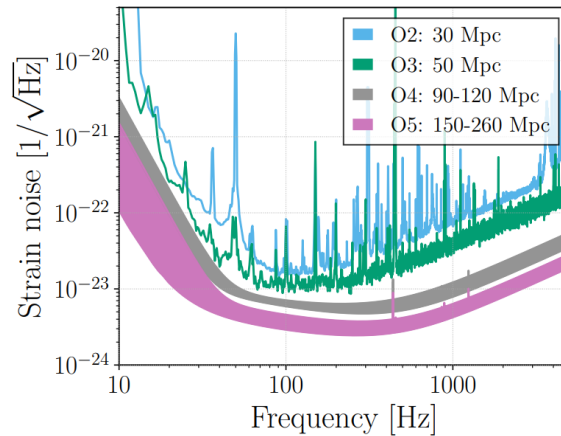


**Figure 1.** Advanced Virgo and Advanced Virgo+ sensitivities from O2 to O5 observation runs, taken from Figure 1 in [10]. The O2 and O3 sensitivity is shown while O4 and O5 give possible ranges depending on outcomes of current studies.

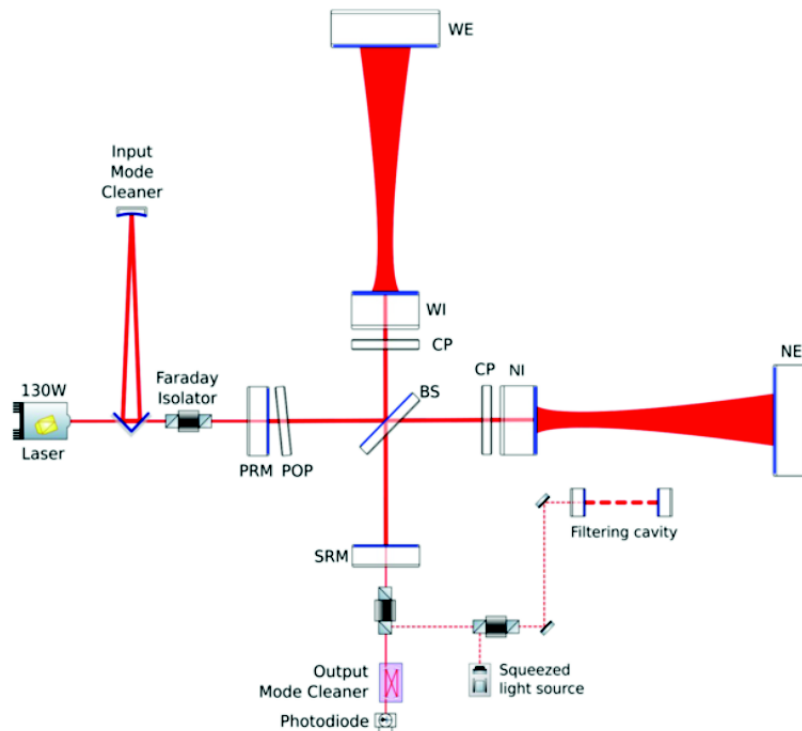


**Figure 2.** AdV+ target optical layout, including the PR mirror (PRM), SR mirror (SRM), beam splitter (BS), and two Fabry–Perot resonant cavities (WI–WE and NI–NE mirrors).

In light of the necessary mirror replacements in Phase II, the goal of this study was to study an optimization of the input mirror (IM), power recycling mirror (PRM), and signal recycling mirror (SRM) transmittances ( $T_{IM}$ ,  $T_{PR}$ , and  $T_{SR}$ , respectively) that fine-tunes the ITF response to astrophysical signals [11].

Currently, mirror transmittances for Phase II (O5) are nominally set to Phase I (O4) values:  $T_{IM}$  at 1.4%,  $T_{PR}$  at 5%, and  $T_{SR}$  at 40%.  $T_{IM}$  was chosen so that the arm-cavity finesse will equal the O3 measured finesse of 450.  $T_{PR}$  was chosen to limit the power recycling gain, thereby reducing wavefront distortions in the power recycling cavity (PRC) and easing requirements on the thermal compensation system accuracy. With these prior selections,  $T_{SR}$  was then set by the choice of input

laser power following a study into detector sensitivity [12,13] as a function of the correlation between these parameters.

Starting from the “nominal” configuration for O5, in this study we explore a larger parameter space: we let all three mirror transmittances vary as we do not assume a strongly over-coupled ITF or a finesse and power recycling gain matching O4. We also explore results for a large range of arm-cavity round trip losses (from 55 ppm to 105 ppm). Moreover, a post-merger (PM) signal (see Section 2 for definition) is used in addition to the usual binary neutron star (BNS) range as a figure of merit for the optimization. Finally, the approach presented in previous work is formalized here using a search algorithm with a specifically developed waveform generator for post-merger signals (in addition to the pre-existing BNS inspiral-merger-ringdown approximant).

The optimization method is explained in Section 2, results are outlined in Sections 3.1 and 3.2, and a comparison drawn between the two sensitivity parameters in Section 3.3. Section 4 then provides some concluding remarks and details future steps.

## 2. Method

Parameters such as mirror RoCs, transmittances, and input laser power defining the possible sensitivity realizations for phase II (O5) are given in Table 1. Two scenarios of O5 high (pessimistic) and O5 low (optimistic) define the violet band extremes in Figure 1. An important parameter is arm cavity round trip losses (RTLs), arising from imperfect mirror surface quality (flatness, roughness, and point defects) and mirror absorption. The nominal RTL value is 85 ppm, but in this work we consider a range of RTLs varying from 55 ppm to 105 ppm since uncertainties still exist on the values achievable for phase II. Concerning other parameters, we assume the ITF to be operating at the O5 low (optimistic) configuration with broadband signal recycling, shown in Figure 3 with a breakdown of limiting noise contributions. The total noise (black) is dominated at higher frequencies by QN only (purple), at mid to low frequencies by QN and coating thermal Brownian noise (red), and at frequencies below 20 Hz by suspension thermal noise (blue). Since optimization of mirror transmittances will only affect the QN curve, which is not the only limitation at mid to low frequencies, it should be possible to find a configuration that fine-tunes high frequency sensitivity with reduced cost to lower frequencies.

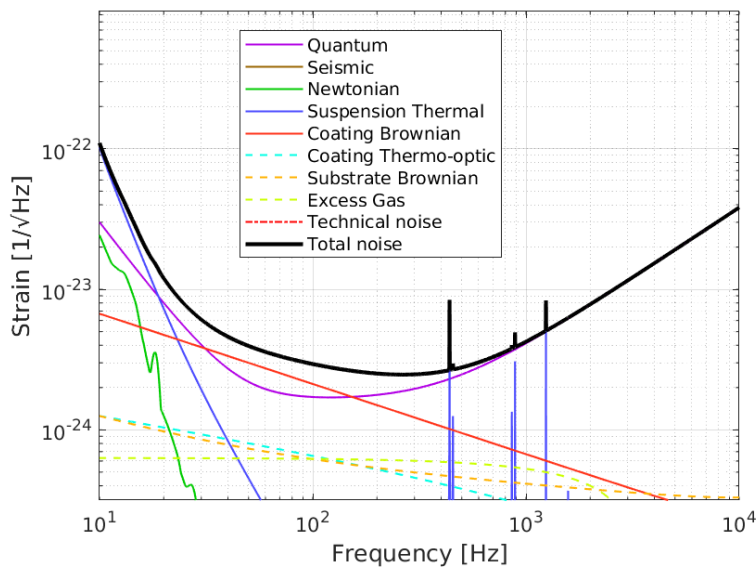


**Figure 3.** Example *low* (optimistic) sensitivity for O5, including breakdown into sub-component contributions.

**Table 1.** Interferometer parameters for phase II of AdV+. The final parameter values and sensitivity curve will depend on photodetector quantum efficiency performance, achievable laser power, and mechanical losses of new coatings used.

Parameter	O5 Low (High)
Laser Power (Leaving IMC) [W]	60 (80)
Produced Squeezing level [dB]	12
Photo-detector quantum efficiency	0.80 (0.93)
PR gain	35
Beam splitter loss	0.0015
Arm cavity beam waist [mm]	7.3
Arm cavity IM to waist [m]	1043
Arm cavity g factor	0.95
Arm cavity RTL [ppm]	85
Power recycling mirror transmittance [%]	5.0
Signal recycling transmittance [%]	40
Input mirror mass [kg]	42
Input mirror radius [cm]	17.5
Input mirror width [cm]	20
Input mirror spot radius [mm]	49
Input mirror RoC [m]	1047
Input mirror transmittance [%]	1.4
End mirror mass [kg]	105
End mirror radius [cm]	27.5
End mirror width [cm]	20
End mirror spot radius [mm]	91
End mirror RoC [m]	1988
End mirror transmittance [%]	$10^{-4}$

A global noise calculator for the AdV and AdV+ detectors advGWINC<sup>1</sup> is used to obtain the AdV+ theoretical sensitivity. Inputting the O5 low parameters to the simulator, an ITF sensitivity is calculated along with leading sub-system contributions and astrophysical figures of merit.

A random walk routine was used to find the transmittances that optimize one of two astrophysical figures of merit (BNS range  $\mathcal{R}$  or PM SNR  $\rho$ ), labeled the ‘primary parameter’. While searching for the optimal transmittances, the sampler takes note of the secondary sensitivity parameter as well as optics parameters such as arm cavity finesse  $\mathcal{F}$ , arm cavity stored power  $P_{Arm}$ , power incident on beam splitter  $P_{BS}$ , PR gain  $G_{PR}$ , and PRC losses  $L_{PRC}$ . A predefined ‘budget’ (a variation window) was allowed around the optimal value so that the sampler filled out correlations between parameters. In each simulation run, the configuration found that gives the optimal primary parameter is labeled ‘opt.’, while the configuration that maximizes the secondary parameter within the predefined budget is labeled ‘max’. For example, when the routine is run to optimize BNS range  $\mathcal{R}$ , the best range found is ‘opt.  $\mathcal{R}$ ’ and the best PM SNR  $\rho$  found within a 3 Mpc budget is ‘max  $\rho$ ’. Conversely, when the routine is run to optimize PM SNR  $\rho$ , the best SNR found is ‘opt.  $\rho$ ’ and the best BNS range  $\mathcal{R}$  found within a 1.5 SNR budget is ‘max  $\mathcal{R}$ ’.

Operating similarly to a Monte Carlo, the random-walk routine draws a point in transmittance space and calls advGWINC to evaluate the ITF sensitivity and its astrophysical figures of merit. It then randomly samples a new trial point close to the current point, and repeats the calculations. For an initial ‘burn in’ period, the trial point is accepted as the new current point only if its primary parameter is larger than at the current point. Once the initial ‘burn in’ period is completed, a trial point is also accepted if its primary parameter is within the error budget of the running global maximum value. If these criteria are not met, then the trial point is discarded and a new point drawn. This is repeated

<sup>1</sup> <https://git.ligo.org/virgo/virgoapp/advgwinc>.

for a large number of draws to produce a chain of accepted points. Once the optimization is completed, points drawn in the initial ‘burn in’ period, where the algorithm is locating the global maximum, are removed from the chain.

The first of the two sensitivity parameters used in this study is BNS inspiral-merger-ringdown (IMR) range  $\mathcal{R}$ . It corresponds to an averaged maximum distance at which a BNS IMR event can be measured [14] with SNR greater than or equal to some pre-defined threshold, assuming a detector with strain noise power spectral density  $S_n(f)$ . It was one of the primary quantifiers of detector sensitivity during the first three observation runs. The advGWINC software approximates this number using an optimally aligned inspiral-merger-ringdown (IMR) waveform produced by IMRPhenomD [15] scaled to a range of redshifts  $z$  to find the cutoff distance where the SNR falls below a threshold  $\rho_0 = 8$ . More precisely, advGWINC defines  $\mathcal{R}$  in frequency space as

$$\mathcal{R} = \frac{2c}{H_0} \left[ \frac{3}{2} \int_0^{z_h} \frac{(\Phi(x_0) - (1+z)^{-1/2}\Phi(x))^2 F_D \left( \Theta_p^2 > \rho_0^2 / \rho^2 \mid z \right) dz}{\Omega_M \sqrt{\Omega_M (1+z)^3 + \Omega_\Lambda}} \right]^{1/3} \quad (1)$$

where  $H_0$  is the Hubble constant,  $c$  the speed of light,  $\Omega_M/\Omega_\Lambda$  the matter/dark energy content of the universe today, and  $z_h$  the redshift horizon (a large upper limit on the integral).  $F_D$  is the probability of a source at a given redshift having SNR greater than the threshold SNR after averaging over angular orientation of the binary orbital plane and sky location [16]. The function  $\Phi$  is a conversion from redshift to luminosity distance [17], and takes the form

$$\Phi(y) = \frac{1 + a_1 y + a_2 y^2 + a_3 y^3}{1 + b_1 y + b_2 y^2 + b_3 y^3} \quad (2)$$

where coefficients  $a_i$  and  $b_i$  are produced by fits to numerical data, and the input variables follow

$$x_0 = \frac{1 - \Omega_M}{\Omega_M} \quad \text{and} \quad x = \frac{x_0}{(1+z)^3} \quad (3)$$

The second optimization parameter used is the SNR  $\rho$  of a BNS post-merger (PM) [18] GW signal, produced by a quasi-stable, rapidly rotating, super/hyper-massive neutron star formed for a fraction of a second or longer after the merger. The objects spin and deformation allow it to emit GWs in the kiloHertz region, making it a complementary sensitivity parameter to  $\mathcal{R}$ . Although other high-frequency astrophysical signals can be used in our optimizations, the successful measurements of BNS events in previous observation runs make PM signals an interesting target.

The SNR of a full BNS event with a PM feature is dominated by the inspiral phase. We therefore restrict our waveform to the PM feature only, similar to Figure 1 in [19], so that there is negligible contribution below  $\sim 1$  kHz and focus is on optimizing PM visibility. Realizations of detector strain noise power spectral density  $S_n$  are combined with a frequency domain waveform  $\tilde{h}(f)$  to give the SNR  $\rho$ , defined by

$$\rho = 2 \left[ \int_{f_0}^{f_1} \frac{|\tilde{h}(f)|^2}{S_n} df \right]^{1/2} \quad (4)$$

where  $[f_0, f_1]$  is the frequency range in which the waveform is computed.

Computation of  $\tilde{h}(f)$  was done by a specialized module added to advGWINC that follows the numerical approximations reported by Breschi et al. [20] and assumes co-aligned spins and ideal binary orientation to the line of sight. Characteristic frequencies and times are calculated with polynomial fits to numerical data for several neutron star equations of state. In this work, the SLy4 equation of state [21] is used for a source with total mass  $(1.364 + 1.364) M_\odot$ . Figure 4 shows the reproduced waveform from the green curves of Figure 5 in [20]. Figure 4a shows the amplitude, angular frequency, and real component of the waveform in geometric units scaled to the total mass. Figure 4b shows the Fourier transform of a time domain waveform (red) assuming a redshift of 0.008, roughly matching the luminosity distance used in the reference, the equivalent IMR waveform with the same redshift

(yellow), and the nominal sensitivity curve (blue). In this example, the O5 low nominal sensitivity curve has a BNS range of 256 Mpc, and the PM waveform has SNR  $\rho = 3.20$ .

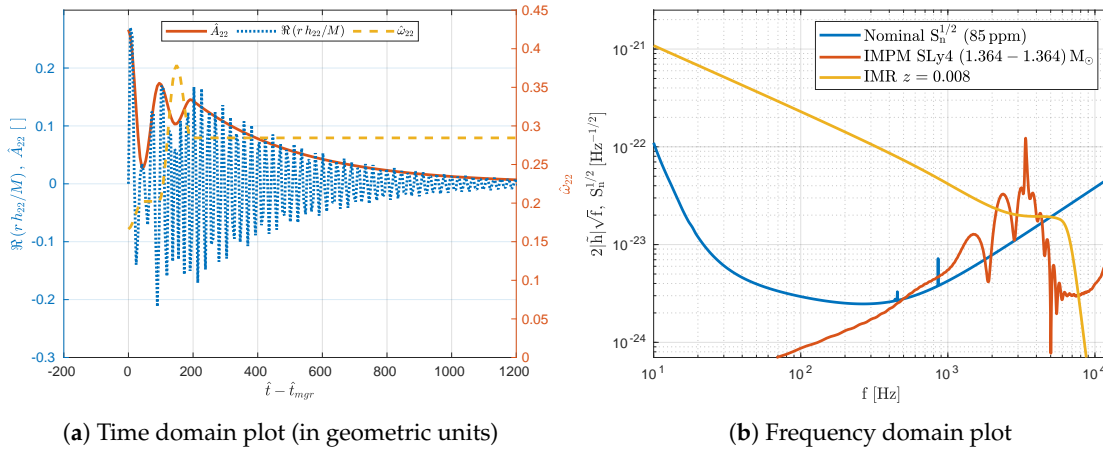


**Figure 4.** (a) Reproduction of time domain post-merger waveform following the numerical model by Breschi et al. [20]. The SLy4 equation of state reported by the authors in the left plot (green curve) of their Figure 5 is reproduced here. Units are geometric and scaled to total binary mass. (b) Frequency domain post-merger only waveform (red) and equivalent binary neutron star (BNS) inspiral-merger-ringdown (IMR) waveform (yellow), both at redshift 0.008. A nominal detector sensitivity with 85 ppm round trip losses is also shown (blue). In this example,  $\rho$  and  $\mathcal{R}$  are 3.20 and 256 Mpc, respectively.

### 3. Results and Discussion

Figure 5 shows values of  $\mathcal{R}$  and  $\rho$ , while Figure 6 shows the corresponding transmittances for each opt and max configuration using budgets of 3 Mpc for  $\mathcal{R}$  and 1.5 SNR for  $\rho$ . Additional parameters linked to the optical system are shown in Figure 7. The reader is directed to Table A1 in Appendix A for numerical values. Simulations were run multiple times to check numerical convergence; each iteration presented some stochastic fluctuation due to finite sampling but asymptotically produced the same results on increasing the number of draws. Simulations were terminated once sensitivity parameters changed by less than 5% on running double the number of draws again.

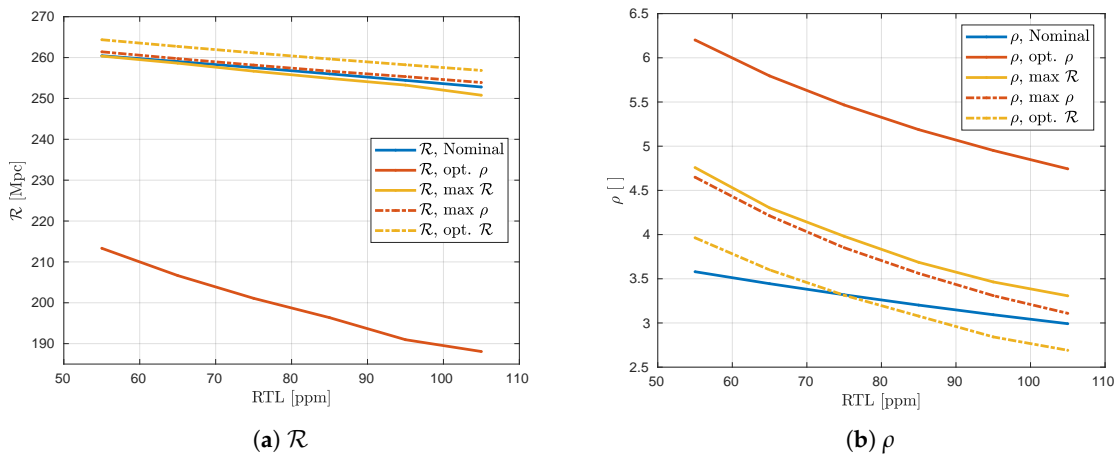


**Figure 5.** Sensitivity parameters as functions of round trip losses (RTLs). ‘Opt’ corresponds to an optimal primary parameter, while ‘max’ corresponds to a maximum secondary parameter within a budget of the optimal primary parameter. Nominal configurations that use the currently expected input mirror (IM), power recycling mirror (PRM), and signal recycling mirror (SRM) transmittances are shown for comparison.

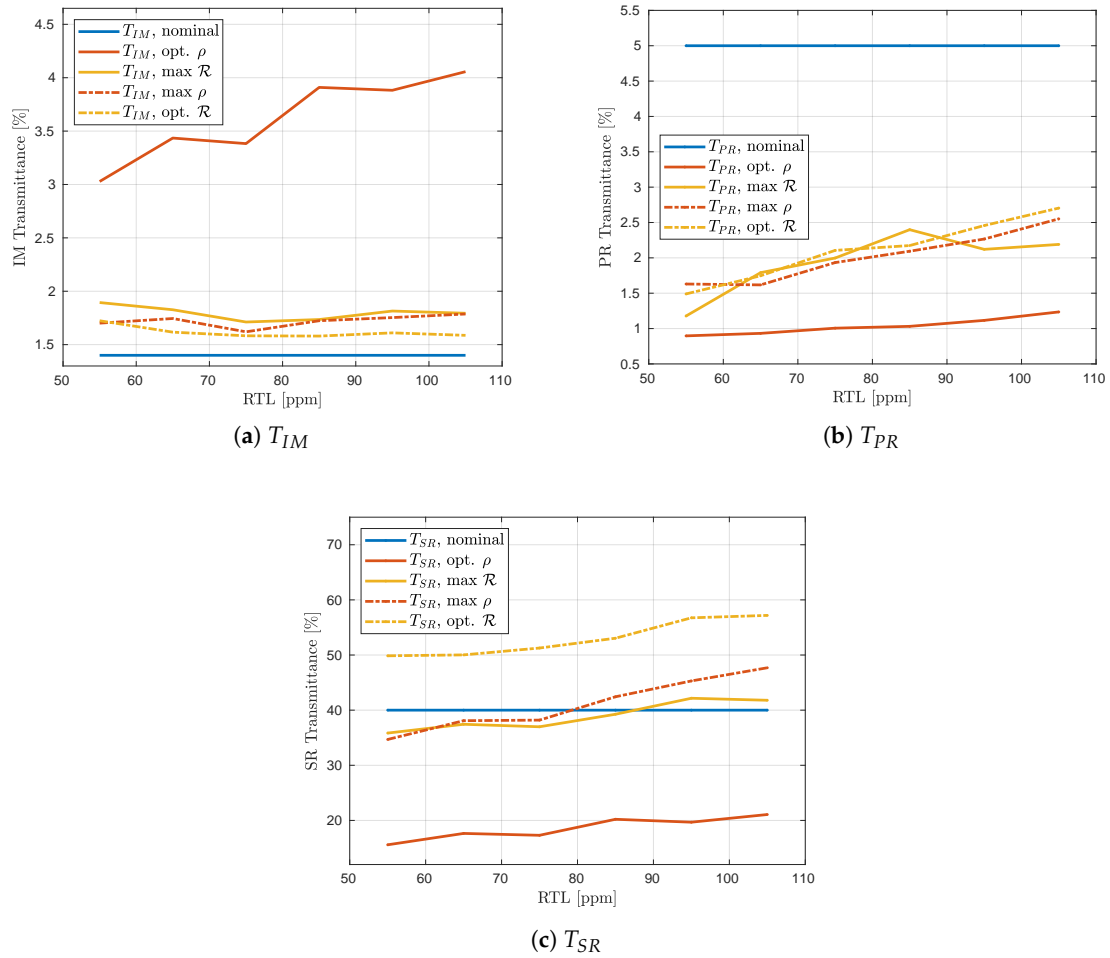


**Figure 6.** Opt and max configuration transmittances found by the optimization routine. ‘Opt’ corresponds to an optimal primary parameter, while ‘max’ corresponds to a maximum secondary parameter within a predefined budget of the optimal primary parameter found. Nominal configurations that use the currently expected IM, PRM, and SRM transmittances are shown for comparison.

### 3.1. Optimizing $\mathcal{R}$

As previously stated, the optimization of BNS range is limited by coating thermal noise that dominates at mid to low frequencies. Hence, the opt.  $\mathcal{R}$  configuration (yellow dot-dashed in Figure 5a) only improves the BNS range by several Mpc from the nominal values (blue). For RTLs of 85 ppm (similar to O3),  $\mathcal{R}$  is improved by 4 Mpc from 256 Mpc to 260 Mpc by marginally increasing  $T_{IM}$ , reducing  $T_{PR}$  from 5% to 2.17%, and increasing  $T_{SR}$  from 40% to 53.0% (as shown in Figure 6). Considering the optical parameters shown in Figure 7, the opt.  $\mathcal{R}$  configuration for 85 ppm RTLs changes the finesse from the nominal 446 to 395, the PR gain from 35 to 44, the arm cavity power from 391 kW to 435 kW, and the recycling cavity power from 2.79 kW to 3.50 kW. The reduced finesse reduces total losses in the arm-cavities which, when coupled with a reduction in  $T_{PR}$ , increases  $G_{PR}$ . Since the proportional increase in  $G_{PR}$  is larger than the proportional drop in  $\mathcal{F}$ , both the arm and recycling cavity powers increase from the nominal stored powers.

Looking now at Figure 5b, the max.  $\rho$  configuration (dot-dashed red) illustrates that there is room for the nominal high frequency sensitivity to be improved. Comparing Figure 5a,b for all RTLs simulated, the max  $\rho$  configuration maintains the nominal  $\mathcal{R}$  while improving the PM SNR  $\rho$ . In fact, for the specific case of 85 ppm, 1 Mpc is added to  $\mathcal{R}$  from the nominal 256 while  $\rho$  is increased from 3.20 to 3.56. This is achieved by decreasing  $T_{SR}$  from 53.0% (opt.  $\mathcal{R}$ ) to 42.4% (max  $\rho$ ), almost meeting the

nominal value of 40%, while keeping  $T_{IM}$  and  $T_{PR}$  relatively unchanged from the opt.  $\mathcal{R}$  configuration. As a result, the optical parameters do not show much change from the opt.  $\mathcal{R}$  configuration, except the finesse  $\mathcal{F}$  that decreases from 396 (opt.  $\mathcal{R}$ ) to 363 (max  $\rho$ ).

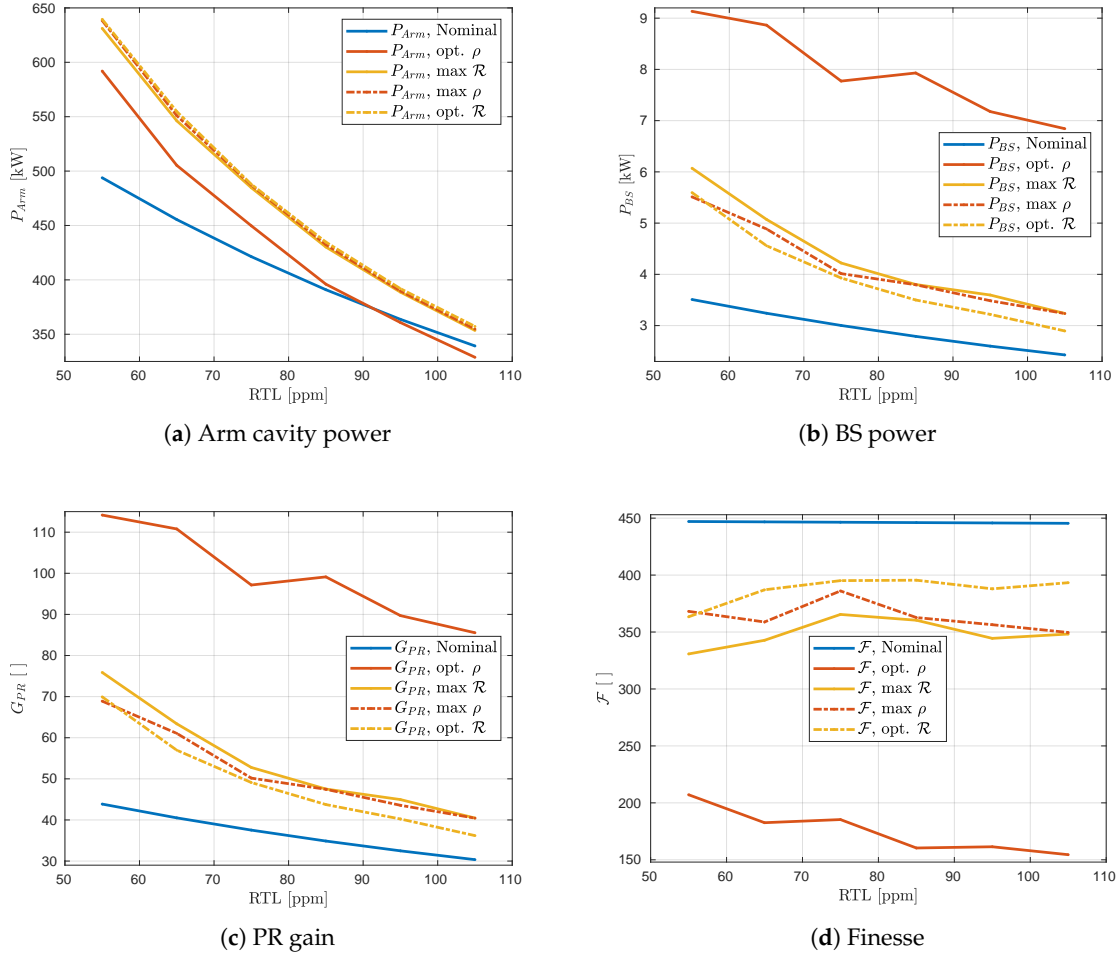


**Figure 7.** Additional parameters calculated by the algorithm but not used in its search criteria. ‘Opt’ corresponds to an optimal primary parameter, while ‘max’ corresponds to a maximum secondary parameter within a predefined budget of the optimal primary parameter found. Nominal configurations that use the currently expected IM, PRM, and SRM transmittances are shown for comparison.

### 3.2. Optimizing $\rho$

Due to QN being the only limitation at high frequencies, the optimization routine can freely change the sensitivity in this region. Indeed, the opt.  $\rho$  configuration (solid red in Figure 5) presents a sharp gain of 62% in  $\rho$  at 85 ppm from 3.20 to 5.19, and a drop of 23% in  $\mathcal{R}$  from 256 Mpc to 196 Mpc, indicating a trade off between high and low frequency sensitivity. For all RTLs, the opt.  $\rho$  configuration has very different transmittances and optical parameters to those found for other configurations, again due to the lack of feedback from lower frequencies in the search algorithm. Figure 6 suggests that, for 85 ppm RTLs, the opt.  $\rho$  configuration is achieved by an increase in  $T_{IM}$  from the nominal 1.4% to 3.91%, a reduction in  $T_{PR}$  from 5% to 1.03%, and a reduction in  $T_{SR}$  from 40% to 20%. Looking at Figure 7, the opt.  $\rho$  configuration shows a marginal increase in arm cavity power from the nominal 391 kW to 396 kW, and a large increase in recycling cavity power from 2.79 kW to 7.93 kW. The PR gain is also increased from 35 to 99 at 85 ppm, while the finesse is reduced from 446 to 160.

Given the opt.  $\rho$  configurations cost to  $\mathcal{R}$  and the drastic changes in optics parameters it presents, a more reasonable fine-tuning of high frequency sensitivity would take into account the cost to low

frequency sensitivity. In Figure 5, the max  $\mathcal{R}$  configuration (solid yellow) shows that this is indeed possible. For the specific case of 85 ppm RTLs,  $\rho$  is decreased from the optimal value of 5.19 to 3.69 while  $\mathcal{R}$  is increased from 196 Mpc to 255 Mpc, just 1 Mpc under the nominal value. Looking at Figure 6, the difference between the max  $\mathcal{R}$  configuration (solid yellow) and the opt.  $\rho$  configuration (solid red) is a decrease in  $T_{IM}$ , increase in  $T_{PR}$ , and an increase in  $T_{SR}$ , for all RTLs. Looking at the specific case of 85 ppm,  $T_{IM}$  is reduced from 3.91% to 1.74%,  $T_{PR}$  is increased from 1.03% to 2.40%, and  $T_{SR}$  is increased from 20% to 39.3%. In Figure 7, the max  $\mathcal{R}$  configuration (solid yellow) has the same optics parameters as the opt.  $\mathcal{R}$  and max  $\rho$  configurations (dot-dashed yellow and red).

### 3.3. Comparing Results

The opt.  $\mathcal{R}$  and opt.  $\rho$  sensitivity curves are shown in Figure 8a along with the nominal sensitivity (blue). While the bucket of the QN curve is greatly enhanced for the opt.  $\mathcal{R}$  configuration (red), the high frequency band is slightly above the nominal curve. In sharp contrast, the opt.  $\rho$  configuration (yellow) shows a greatly reduced high frequency noise at the cost of sensitivity in the bucket. In contrast, the max  $\rho$  and max  $\mathcal{R}$  sensitivities shown in Figure 8b almost overlap. Compared to the blue nominal curve, there is a noticeable reduction in high frequency noise in both cases while the mid frequency sensitivity is almost unchanged. This further shows the potential to gain sensitivity at high frequencies without compromising low frequency performance.

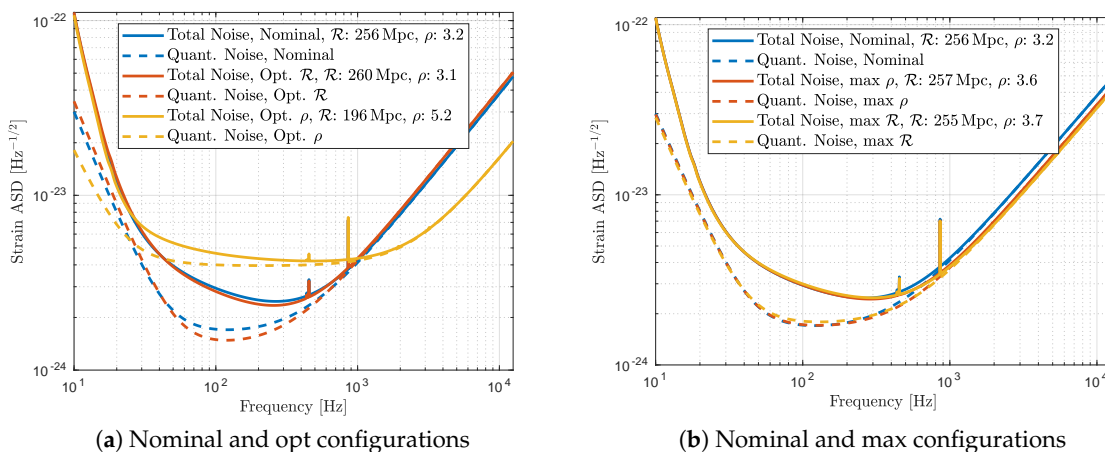


**Figure 8.** Sensitivity curves for 85 ppm RTL optimal and max parameter configurations found for both optimization routines. ‘Opt’ corresponds to an optimal primary parameter, while ‘max’ corresponds to a maximum secondary parameter within a predefined budget of the optimal primary parameter found. Nominal configurations that use the currently expected IM, PRM, and SRM transmittances are shown for comparison.

Figure 9 shows correlations found for 85 ppm RTLs between the two figures of merit and transmittances using budgets of 3 Mpc for  $\mathcal{R}$  (green) and 1.5 SNR for  $\rho$  (black). There is a clear change in correlations depending on choice of primary parameter, and a filled parabolic trade-off between  $\mathcal{R}$  and  $\rho$  indicated by the bottom right plot, which is enlarged in Figure (BLAH). Color points show the opt.  $\mathcal{R}$  (open red), max  $\rho$  (open yellow), opt.  $\rho$  (solid yellow), max  $\mathcal{R}$  (solid red), and nominal (blue) configurations. Transmittances are in log scale. Note the near overlap of max  $\rho$  (open yellow) and max  $\mathcal{R}$  (solid red) points, indicating again the equivalence between these configurations.

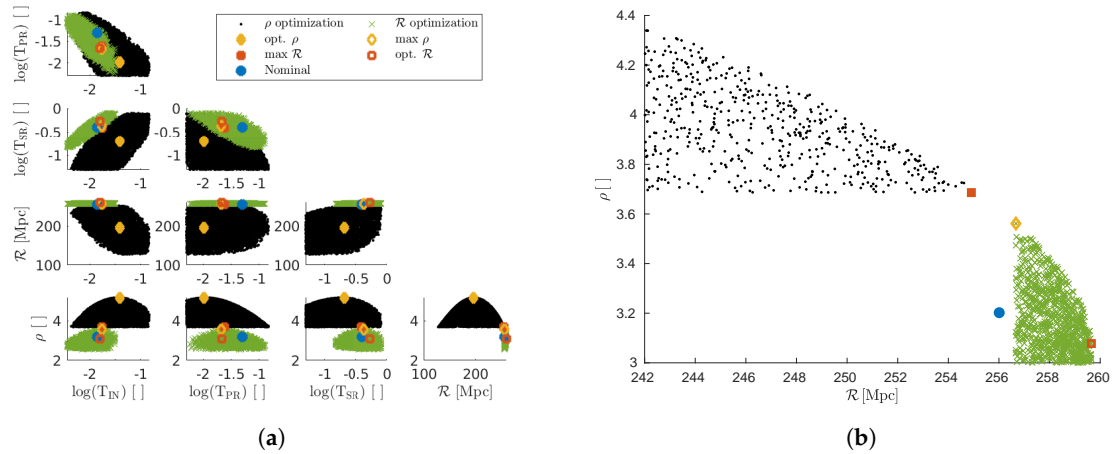


**Figure 9.** (a) Correlations found for 85 ppm RTLs.  $\mathcal{R}$  (green) uses 3 Mpc budget and  $\rho$  (black) uses 1.5 SNR budget. Color points indicate nominal configuration (blue), opt.  $\mathcal{R}$  (open red), max  $\rho$  (open yellow), opt.  $\rho$  (solid yellow), and max  $\mathcal{R}$  (solid red). (b) Enlargement of  $\mathcal{R}$  and  $\rho$  plot (bottom right of corner plot).

Assuming similar RTLs to those measured in O3 of 85 ppm, the max  $\mathcal{R}$  configuration gives a 15% increase in  $\rho$  from SNR 3.20 to 3.69 at the cost of 1 Mpc to  $\mathcal{R}$  now at 255 Mpc. The corresponding transmittances to achieve this configuration move the nominal values from 1.4%, 5%, and 40% to 1.74%, 2.40%, and 39.3% for  $T_{IM}$ ,  $T_{PR}$ , and  $T_{SR}$ , respectively.

### 3.4. Stability of Results with Arm-Cavity Losses

Uncertainties exist on RTLs for O5 and there is a strong dependence of the optimal and max configurations on RTLs. A check was done to investigate the effects of implementing the max  $\mathcal{R}$  configuration transmittances found with 85 ppm RTLs, in ITFs with 55 ppm and 105 ppm RTLs. For 55 ppm, the sensitivity parameters  $\mathcal{R}$  and  $\rho$  were changed from 255 Mpc and 3.69 SNR to 262 Mpc and 4.31 SNR, respectively. For 105 ppm,  $\mathcal{R}$  and  $\rho$  were changed to 250 Mpc and 3.36 SNR. These correspond to a gain of 7 Mpc and 0.62 SNR if the RTLs are better than expected, and a loss of 5 Mpc and 0.33 SNR if the RTLs are worse than expected.

This was then repeated for the nominal configuration. For 55 ppm,  $\mathcal{R}$  and  $\rho$  were changed from 256 Mpc and 3.20 SNR to 260 Mpc and 3.58 SNR. For 105 ppm,  $\mathcal{R}$  and  $\rho$  were changed to 253 Mpc and 2.99 SNR. This is a gain of 4 Mpc and 0.38 SNR for a better than expected RTL, and a loss of 3 Mpc and 0.21 SNR if the RTLs are worse than expected.

Table 2 shows the values of  $\mathcal{R}$  and  $\rho$  when the transmittances for the max  $\mathcal{R}$  or nominal configurations with 85 ppm RTLs are implemented in ITFs with 55 ppm or 105 ppm RTLs. The potential change in both  $\mathcal{R}$  and  $\rho$  are larger for the max  $\mathcal{R}$  configuration than the nominal configuration. In both cases, the potential gain is larger than the potential loss. The max  $\mathcal{R}$  configuration, however, shows a larger potential gain than the nominal configuration.

**Table 2.** Astrophysical figures of merit using transmittances found for the max  $\mathcal{R}$  configuration with 85 ppm in interferometers (ITFs) with RTLs indicated by column headers.

Figure of Merit	Nominal			max $\mathcal{R}$		
	55 ppm	85 ppm	105 ppm	55 ppm	85 ppm	105 ppm
$\mathcal{R}$ [Mpc]	260	256	253	262	255	250
$\rho$ [SNR]	2.58	3.20	2.99	4.31	3.69	3.36

#### 4. Conclusions and Future Steps

In this work, we have investigated the optimization of the sensitivity of the Advanced Virgo+ phase II detector (corresponding to the O5 observation run) by changing the interferometer mirror transmittances and using a random walk algorithm. A post-merger SNR  $\rho$  was used for the optimization in addition to the usual IMR range  $\mathcal{R}$ . The two figures of merit roughly correspond to high-frequency and mid frequency signals, respectively.

It was found that, assuming arm cavity RTLs similar to O3 around 85 ppm, independent of choice of primary optimization parameter ( $\rho$  or  $\mathcal{R}$ ), a configuration could be identified that enhanced the high frequency sensitivity without compromising the foreseen performance at low frequencies. This configuration, labeled ‘max  $\mathcal{R}$ ’ in this paper, would set  $T_{IM}$ ,  $T_{PR}$ , and  $T_{SR}$  to 1.74%, 2.40%, and 39.3%.

This configuration was checked for stability against measured losses different than those assumed in the study of 85 ppm. In this respect, the max  $\mathcal{R}$  configuration poses a slightly higher risk if RTLs are larger than expected, but a much larger pay-off if RTLs are smaller than expected.

A detailed study of the control system should be made before making a decision on the final configuration. For instance, since the optimized configuration found in this work corresponds to an increase in recycling gain, additional difficulties can arise for the control systems of the marginally stable recycling cavities. In addition, since power is significantly redistributed between the nominal and max configurations, the perturbation to mirror RoCs due to thermal loads should be checked against thermal compensation system ranges. Moreover, this study was done in the context of a broadband signal recycling configuration, but can be continued to include a tuned configuration.

In the future, we plan to perform a qualification of the gains in sensitivity in the context of parameter estimation. A change in  $\rho$  could be converted to a change in posterior error on a parameter proposed in the literature like  $\zeta$  [22] that includes information on the equation of state. This would permit a more quantitative comparison between proposed gains in  $\rho$  to proposed losses in  $\mathcal{R}$ .

Although this work was carried out in the context of the AdV+ phase II upgrades, the methods used would be useful to future optimization studies, such as fine-tuning the sensitivity for future gravitational-wave detectors like Einstein Telescope [23] and Cosmic Explorer [24]. In the context of these detectors, that are expected to extract PM features, a study of this kind would be highly informative to compare the risks and gains of each optical design.

**Author Contributions:** Investigation, J.B. and M.B.; writing—original draft preparation, J.B.; writing—review and editing, J.B. and M.B. All authors have read and agreed to the published version of the manuscript.

**Funding:** J.B. supported by the European Gravitational Observatory.

**Acknowledgments:** The authors acknowledge the useful feedback and discussions with Eleonora Capocasa, Jérôme Degallaix, Sebastian Steinlechner, Gianluca Gemme, Alessio Rocchi, Eric Chassande-Mottin, Simone Mastrogiovanni and the developers of the advGWINC code. The authors also acknowledge the useful work by Breschi et al. and the helpful communications in developing a dedicated PM waveform module within advGWINC.

**Conflicts of Interest:** The authors declare no conflict of interest. The funders had no role in the design of the study; in the collection, analyses, or interpretation of data; in the writing of the manuscript, or in the decision to publish the results.

#### Abbreviations

The following abbreviations are used in this manuscript:

ITF	Interferometer
AdV	Advanced Virgo
AdV+	Advanced Virgo+
QN	quantum noise
IM	input mirror
EM	end mirror

PRM	power recycling mirror
SRM	signal recycling mirror
PRC	power recycling cavity
$T_{IM}$	input mirror transmittance
$T_{PR}$	power recycling mirror transmittance
$T_{SR}$	signal recycling mirror transmittance
PM	post-merger
IMR	inspiral-merger-ringdown
BNS	binary neutron star
SNR	signal to noise ratio
RTL	round trip losses
$\mathcal{R}$	BNS IMR range
$\rho$	BNS PM SNR
GW	gravitational wave
RoC	radius of curvature

## Appendix A

**Table A1.** Optimization results for six values of round trip losses for the two primary parameters  $\mathcal{R}$  and  $\rho$ . Shown are the configurations for optimal  $\mathcal{R}$  ( $\rho$ ), maximum  $\rho$  ( $\mathcal{R}$ ) within  $\pm 3$  Mpc ( $\pm 15$  SNR) of the optimal primary parameter, and nominal configurations, where colours indicated correspond to curves plotted in Figures 5 and 6 Also shown are the corresponding Finesse ( $F$ ), power recycling gain ( $G_{PR}$ ), PRC losses ( $L_{PRC}$ ), arm cavity power ( $P_{Arm}$ ), and power impinging on the beam splitter ( $P_{BS}$ ).

	RTL	Conf.	$\mathcal{R}$ [Mpc]	$\rho$	$T_{IM}$ [%]	$T_{PR}$ [%]	$T_{SR}$ [%]	$\mathcal{F}$	PR Gain	$L_{PRC}$ [%]	$P_{Arm}$ [kW]	$P_{BS}$ [kW]
$\mathcal{R}$ Opt.	55 ppm	Nom (blue)	260	3.58	1.40	5.00	40.0	447	44	1.55	494	3.51
		opt $\mathcal{R}$ (red)	264	3.96	1.72	1.49	49.9	363	70	1.26	640	5.60
		max $\rho$ (yellow)	261	4.65	1.70	1.63	34.7	368	69	1.27	638	5.51
	65 ppm	Nom (blue)	259	3.44	1.40	5.00	40.0	447	41	1.83	455	3.24
		opt $\mathcal{R}$ (red)	263	3.60	1.62	1.75	50.0	387	57	1.58	555	4.56
		max $\rho$ (yellow)	260	4.21	1.74	1.62	38.1	359	61	1.47	551	4.88
	75 ppm	Nom (blue)	258	3.32	1.40	5.00	40.0	446	38	2.11	421	3.00
		opt $\mathcal{R}$ (red)	261	3.31	1.58	2.11	51.3	395	49	1.86	488	3.93
		max $\rho$ (yellow)	258	3.85	1.62	1.93	38.2	386	50	1.82	487	4.01
	85 ppm	Nom (blue)	256	3.20	1.40	5.00	40.0	446	35	2.38	391	2.79
		opt $\mathcal{R}$ (red)	260	3.08	1.58	2.17	53.0	396	44	2.11	435	3.50
		max $\rho$ (yellow)	257	3.56	1.72	2.09	42.4	363	47	1.94	432	3.80
	95 ppm	Nom (blue)	254	3.09	1.40	5.00	40.0	446	32	2.66	364	2.60
		opt $\mathcal{R}$ (red)	258	2.84	1.61	2.46	56.7	388	40	2.31	392	3.22
		max $\rho$ (yellow)	255	3.31	1.75	2.27	45.3	356	44	2.13	390	3.49
	105 ppm	Nom (blue)	253	2.99	1.40	5.00	40.0	445	30	2.94	339	2.43
		opt $\mathcal{R}$ (red)	257	2.69	1.59	2.70	57.2	393	36	2.59	357	2.90
		max $\rho$ (yellow)	254	3.11	1.79	2.55	47.7	350	40	2.30	355	3.24

Table A1. Cont.

RTL	Conf.	$\mathcal{R}$ [Mpc]	$\rho$	$T_{IM}$ [%]	$T_{PR}$ [%]	$T_{SR}$ [%]	$\mathcal{F}$	PR Gain	$L_{PRC}$ [%]	$P_{Arm}$ [kW]	$P_{BS}$ [kW]	
$\rho$ Opt.	55 ppm	Nom (blue)	260	3.58	1.40	5.00	40.0	447	44	1.55	494	3.51
		opt $\rho$ (red)	213	6.20	3.03	0.90	15.6	207	114	0.71	592	9.13
		max $\mathcal{R}$ (yellow)	260	4.76	1.89	1.18	35.8	330	76	1.14	631	6.07
	65 ppm	Nom (blue)	259	3.44	1.40	5.00	40.0	447	41	1.83	455	3.24
		opt $\rho$ (red)	207	5.80	3.43	0.93	17.6	183	111	0.74	505	8.86
		max $\mathcal{R}$ (yellow)	259	4.30	1.83	1.79	37.4	343	63	1.40	546	5.07
	75 ppm	Nom (blue)	258	3.32	1.40	5.00	40.0	446	38	2.11	421	3.00
		opt $\rho$ (red)	201	5.47	3.38	1.01	17.3	185	97	0.87	450	7.77
		max $\mathcal{R}$ (yellow)	257	3.98	1.71	2.00	37.0	365	53	1.72	485	4.22
	85 ppm	Nom (blue)	256	3.20	1.40	5.00	40.0	446	35	2.38	391	2.79
		opt $\rho$ (red)	196	5.19	3.91	1.03	20.0	160	99	0.85	396	7.93
		max $\mathcal{R}$ (yellow)	255	3.69	1.74	2.40	39.3	360	48	1.92	430	3.80
	95 ppm	Nom (blue)	254	3.09	1.40	5.00	40.0	446	32	2.66	364	2.60
		opt $\rho$ (red)	191	4.95	3.88	1.12	19.7	161	90	0.96	361	7.18
		max $\mathcal{R}$ (yellow)	253	3.46	1.81	2.12	42.2	344	45	2.05	389	3.60
	105 ppm	Nom (blue)	253	2.99	1.40	5.00	40.0	445	30	2.94	339	2.43
		opt $\rho$ (red)	188	4.74	4.06	1.24	21.1	154	86	1.01	329	6.84
		max $\mathcal{R}$ (yellow)	251	3.31	1.79	2.19	41.8	348	40	2.29	354	3.24

## References

- Abbott, B. et al. [LIGO Scientific Collaboration and Virgo Collaboration]. Observation of gravitational waves from a binary black hole merger. *Phys. Rev. Lett.* **2016**, *116*, 061102. [\[CrossRef\]](#)
- Abbott, R. et al. [LIGO Scientific Collaboration and Virgo Collaboration]. GWTC-2: Compact Binary Coalescences Observed by LIGO and Virgo During the First Half of the Third Observing Run. *arXiv* **2020**, arXiv:2010.14527.
- Abbott, R. et al. [LIGO Scientific Collaboration and Virgo Collaboration]. GW190412: Observation of a binary-black-hole coalescence with asymmetric masses. *Phys. Rev. D* **2020**, *102*, 043015. [\[CrossRef\]](#)
- Abbott, B. et al. [LIGO Scientific Collaboration and Virgo Collaboration]. GW190425: Observation of a Compact Binary Coalescence with Total Mass  $\sim 3.4 M_{\odot}$ . *Astrophys. J. Lett.* **2020**, *892*, L3. [\[CrossRef\]](#)
- Abbott, R. et al. [LIGO Scientific Collaboration and Virgo Collaboration]. GW190814: Gravitational Waves from the Coalescence of a 23 Solar Mass Black Hole with a 2.6 Solar Mass Compact Object. *Astrophys. J. Lett.* **2020**, *896*, L44. [\[CrossRef\]](#)
- Abbott, R. et al. [LIGO Scientific Collaboration and Virgo Collaboration]. GW190521: A Binary Black Hole Merger with a Total Mass of  $150 M_{\odot}$ . *Phys. Rev. Lett.* **2020**, *125*, 101102. [\[CrossRef\]](#)
- Abbott, R. et al. [LIGO Scientific Collaboration and Virgo Collaboration]. Properties and Astrophysical Implications of the  $150 M_{\odot}$  Binary Black Hole Merger GW190521. *Astrophys. J. Lett.* **2020**, *900*, L13. [\[CrossRef\]](#)
- Acernese, F. et al. [Virgo Collaboration]. Advanced Virgo: A second-generation interferometric gravitational wave detector. *Class. Quant. Grav.* **2015**, *32*, 024001. [\[CrossRef\]](#)
- Accadia, T. et al. [Virgo Collaboration]. Virgo: A laser interferometer to detect gravitational waves. *J. Instrum.* **2012**, *7*, P03012.
- Abbott, B. et al. [KAGRA Collaboration, LIGO Scientific Collaboration and Virgo Collaboration]. Prospects for observing and localizing gravitational-wave transients with Advanced LIGO, Advanced Virgo and KAGRA. *Living Rev. Relativ.* **2018**, *21*, 3. [\[CrossRef\]](#)
- Mizuno, J.; Strain, K.A.; Nelson, P.G.; Chen, J.M.; Schilling, R.; Rudiger, A.; Winkler, W.; Danzmann, K. Resonant sideband extraction: A new configuration for interferometric gravitational wave detectors. *Phys. Lett. A* **1993**, *175*, 273–276. [\[CrossRef\]](#)
- Barsotti, L.; Evans, M.; Fritschel, P. aLIGO ISC design study for low power operation. *LIGO Tech. Note* **2012**, T1200128-v4.

13. Gemme, G.; Bertolini, A.; Degallaix, J.; Eisenmann, M.; Was, M. SR Mirror Reflectivity Choice for O4. *Intern. Opt. Study* **2019**. Available online: <https://wiki.virgo-gw.eu/AdvancedVirgoPlus/SRMirrorReflectivity> (accessed on 7 December 2020).
14. Miller, J. On the inspiral range. *LIGO Tech. Note* **2016**, LIGO-T1500491-v2.
15. Khan, S.; Husa, S.; Hannam, M.; Ohme, F.; Purrer, M.; Forteza, X.J.; Bohe, A. Frequency-domain gravitational waves from nonprecessing black-hole binaries. II. A phenomenological model for the advanced detector era. *Phys. Rev. D* **2016**, *93*, 044007. [[CrossRef](#)]
16. Sutton, P. A Rule of Thumb for the Detectability of Gravitational-Wave Bursts. *arXiv* **2013**, arXiv:1304.0210.
17. Adachi, M.; Kasai, M. An Analytical Approximation of the Luminosity Distance in Flat Cosmologies with a Cosmological Constant. *Prog. Theor. Phys.* **2012**, *127*, 145–152. [[CrossRef](#)]
18. Shibata, M. Merger of binary neutron stars: Gravitational waves and electromagnetic counterparts. *Nucl. Phys.* **2016**, *956*, 225–232. [[CrossRef](#)]
19. Chatziioannou, K.; Clark, J.A.; Bauswein, A.; Millhouse, M.; Littenberg, T.B.; Cornish, N. Inferring the post-merger gravitational wave emission from binary neutron star coalescences. *Phys. Rev. D* **2017**, *96*, 124035. [[CrossRef](#)]
20. Breschi, M.; Bernuzzi, S.; Zappa, F.; Agathos, M.; Perego, A.; Radice, D.; Nagar, A. Kilohertz gravitational waves from binary neutron star remnants: Time-domain model and constraints on extreme matter. *Phys. Rev. D* **2019**, *100*, 104029. [[CrossRef](#)]
21. Shabanat, E.; Bonche, P.; Haensel, P.; Meyer, J.; Schaeffer, R. Erratum to “A Skyrme parametrization from subnuclear to neutron star densities. (II): Nuclei far from stabilities” [Nucl. Phys. A 635 (1998) 231–256]. *Nucl. Phys. A* **1998**, *643*, 441.
22. Tsang, K.; Dietrich, T.; Van Den Broeck, C. Modeling the postmerger gravitational wave signal and extracting binary properties from future binary neutron star detections. *Phys. Rev. D* **2019**, *100*, 044047. [[CrossRef](#)]
23. Maggiore, M.; Van Den Broeck, C.; Bartolo, N.; Belgacem, E.; Bertacca, D.; Bizouard, M.A.; Branchesi, M.; Clesse, S.; Foffa, S.; Garcia-Bellido, J.; et al. Science case for the Einstein telescope. *J. Cosmol. Astropart. Phys.* **2020**, *2020*, 50. [[CrossRef](#)]
24. Reitze, D.; Adhikari, R.X.; Ballmer, S.; Barish, B.; Barsotti, L.; Billingsley, G.; Brown, D.A.; Chen, Y.; Coyne, D.; Eisenstein, R.; et al. Cosmic Explorer: The U.S. Contribution to Gravitational-Wave Astronomy beyond LIGO. *Bull. Am. Astron. Soc.* **2019**, *51*, 35.

**Publisher’s Note:** MDPI stays neutral with regard to jurisdictional claims in published maps and institutional affiliations.



© 2020 by the authors. Licensee MDPI, Basel, Switzerland. This article is an open access article distributed under the terms and conditions of the Creative Commons Attribution (CC BY) license (<http://creativecommons.org/licenses/by/4.0/>).